Hydraulic Fracture Height Growth Under the Combined Influence of Stress Barriers and Natural Fractures

J. Huang, J. P. Morris, P. Fu, R. R. Settgast, C. S. Sherman, F. J. Ryerson

January 31, 2018

SPE Journal

Hydraulic Fracture Height Growth Under the Combined Influence of Stress Barriers and Natural Fractures

Jixiang Huang, Joseph P. Morris, Pengcheng Fu, Randolph R. Settgast, Christopher S. Sherman, Frederick J. Ryerson

Lawrence Livermore National Laboratory

Abstract

A fully coupled finite element/finite volume code is used to model 3D hydraulically driven fractures under the influence of strong vertical variations in closure stress interacting with natural fractures. Previously-unknown 3D interaction mechanisms on fracture height growth are revealed. Slipping of a natural fracture, triggered by elevated fluid pressure from an intersecting hydraulic fracture, can induce both increases and decreases of normal stress in the minimum horizontal stress direction, toward the center and tip of the natural fracture, respectively. Consequently, natural fractures are expected to be able to both encourage and inhibit the progress of hydraulic fractures propagating through stress barriers, depending upon the relative locations between the intersecting fractures. Once the hydraulic fracture propagates above the stress barrier through the weaken segment near a favorably located natural fracture, a configuration consisting of two opposing fractures cutting the stress barrier from above and below forms. The fluid pressure required to break the stress barrier under such opposing-fracture configurations is substantially lower than that required by a fracture penetrating the same barrier from one side. Sensitivity studies of geologic conditions and operational parameters have also been performed to explore the feasibility of controlled fracture height. The interactions between hydraulic fractures, natural fractures, and geologic factors such as stress barriers in 3D are shown to be much more complex than in 2D. Although it is impossible to exhaust all the possible configurations, the ability of a 3D, fully coupled numerical model to naturally capture these processes is well demonstrated.

Introduction

Factors controlling hydraulic fracture height growth have been widely discussed in the literature (Naceur and Touboul, 1990). Among them, *in situ* stress contrast between adjoining layers is recognized as one of the principal mechanisms that contain fractures in most scenarios. This is attributed to the fact that source rock reservoirs are heterogeneous at very fine scales as a consequence of depositional sequence and subsequent compaction. The resultant heterogeneity in elastic properties can potentially induce large variations in lateral *in situ* stress from one narrow vertical interval to the next within a pay zone because the same tectonic strains could induce significantly different stress states within each layer (Eaton, 1969). When a hydraulic fracture reaches a horizon where the stress contrast is high, it might not have the net pressure necessary for propagating into the higher-stress layer (Simonson et al., 1978). For normal and strike-slip stress environments, the hydraulic fracture opens against the minimum horizontal stress and propagation is largely within a vertical plane with the minimum horizontal stress controlling vertical propagation. This phenomenon has been confirmed both through modeling and laboratory experiment (Jeffrey and Bunger, 2009). Consequently, hydraulic fracturing in source rocks can be strongly influenced by narrow bands of closure stress contrast induced by heterogeneity.

On the other hand, many source rock plays have been also observed to contain dense networks of natural fractures that are believed to alter the propagation pattern of hydraulic fractures (Gale et al., 2015). Different from faults, natural fractures, including both tensile fractures (i.e. joints) and shear fractures, are the cracks or surfaces of breakage along which there has been no observable movement (Engelder et al., 2009). It is generally believed that natural fractures are ubiquitous in shale plays. From the perspective of production mechanism in low-permeability shale reservoir, natural fractures are critical to production since the formations are so tight that hydrocarbon can be produced only when extensive networks of natural fractures exist (Carlson and Mercer, 1991). The natural fractures that are well filled with calcite or other minerals (named as veins in structural geology) and potentially to be activated during the hydraulic fracturing treatment could complicate the reservoir stimulation in unexpected ways. The simple but efficient boundary element method has been extensively used to simulate the interaction between hydraulic and natural fractures under homogeneous linear elastic reservoir conditions (e.g., Weng et al., 2011; McClure and Horne, 2013; Wu and Olson, 2016; Sesetty and Ghassemi, 2017). More advanced numerical methods have also been extended with the capabilities to simulate the fracture interaction under complex geological settings, including both continuum and discontinuum models (e.g., Fu et al., 2013; Dahi-Taleghani and Olson, 2013; Zhou et al., 2015; Zhou et al., 2016; Chen et al., 2017; Zhang et al., 2017). For instance, Fu et al. (2013) developed an explicitly integrated finite element/finite volume approach with adaptive remeshing for simulating hydraulic fracturing in arbitrary fracture networks; Dahi-Taleghani and Olson (2013) presented an extended finite element method (XFEM) that can simulate the diversion of hydraulic fracture path along natural fractures; Zhou et al. (2017) developed a novel dual-lattice discrete element model to significantly improve the understandings of discontinuous behaviors of rocks that cannot be adequately modeled by continuum models.

Although numerous studies have investigated the effect of vertically oriented natural fractures upon hydraulic fracture growth, the bulk of these studies have considered the special scenario where the vertical extents of the hydraulic fracture, pay zone and natural fractures are identical (e.g., Renshaw and Pollard, 1995; Zhang and Jeffrey, 2008). By doing so, the dimensionality of the problem is reduced to 2D, making both experiment and modeling simpler. Such studies have demonstrated conditions where a hydraulic fracture is arrested at a natural fracture and a fracture crosses a natural fracture either through a direct intersection or an indirect intersection with an “offset” (e.g., Gu et al., 2012; Guo et al., 2015; Taleghani and Olson, 2013; Potluri et al., 2005). However, this rather limited set of interaction modes between hydraulic fractures and natural fractures is a direct consequence of the 2D assumption. In contrast, natural fractures in a real pay zone are quite likely to only span a fraction of the entire heights of the pay zone. This makes possible many modes of interactions between fractures and the formation that are more realistic and more complex.

An earlier study has demonstrated that a hydraulic fracture is able to bypass an uncemented natural fracture (Fu et al., 2015), consistent with experimental observations (Bahorich et al., 2012; Fu et al., 2016). In the current study, we aim to investigate hydraulic fracture height growth in source rocks under the combined influence of narrow bands of closure stress contrast and vertically oriented natural fractures. In particular, a mechanism through which the slipping of a natural fracture enables the hydraulic fracture to break through a thin, high-stress layer that the hydraulic fracture could not break otherwise will be investigated. An extensively validated 3D hydraulic fracturing simulator that can model arbitrary geometries of fractures and arbitrary distributions of in situ stresses is used as the main tool of study.

The present paper is composed of three main sections. The first section is devoted to the discussions and verification of the fracturing criterion used in the numerical model. Analytical solutions along with an energy-based numerical method are used to show its validity near stress barrier. In the second part of the paper, we focus on a baseline simulation to demonstrate how a hydraulic fracture’s height growth into a stress barrier is influenced by natural fractures. Following that, we illustrate the two main contributing mechanisms that assist the breakthrough of stress barrier, through a series of sensitivity studies on the geological conditions and operational parameters.

Modeling Approach

Hydraulic fracture propagation is a coupled multi-physics process involving the deformation of the rock body, fluid flow along existing fractures and in the rock body, as well as the extension of fractures. Therefore, a fully coupled hydraulic fracture simulation code GEOS, developed at the Lawrence Livermore National Laboratory (Settgast et al., 2014, 2017), is employed as the primary tool for the current study. To simulate hydraulic fracturing, GEOS couples a finite element method (FEM) for mechanical response of the solid matrix, a finite volume method (FVM) based on lubrication theory for the fluid flow along fractures, and the linear elastic fracture mechanics (LEFM) for the fracturing criterion. FVM is also used in GEOS to model porous medium flow in the rock matrix, but that module is not invoked in the current study as matrix flow does not play a significant role in the phenomena being studied. Arbitrary configurations of interacting fractures and geologic formations can be accommodated to the extent that meshing permits. The FEM and FVM are naturally coupled: the fluid pressure from the flow module is applied to the surface of the fracture in the solid mesh, while the solid deformation determines the aperture (which in turn determines hydraulic impedance and storage) of the fracture. Fracture propagation is modeled by mesh splitting, governed by energy-based fracturing criterion with the fracture energy release rate computed using a modified version of the virtual crack closure technique (MVCCT: original formulation in Krueger 2004 and modified formulation to consider confining stress in Settgast et al. 2017). The MVCCT approach of modeling hydraulic fracturing yields a robust method that scales well to a large number of processors, enabling the handling of large and complex problems ranging from near-wellbore effects (Sherman et al., 2015) to full field-scale calculation involving well-to-well interactions (Izadi et al., 2015). The formulation of GEOS's hydraulic fracturing module as well as extensive verification and validation studies have been reported in Fu et al. (2013) and Settgast et al. (2017), and thus not repeated here. We focus on the method of modeling natural fractures in this section, which plays a central role in the present work but has not been documented in detail previously, followed by the validity check of MVCCT through a verification case directly relevant to the phenomenon being studied.

Modeling natural fractures

In GEOS, both natural fractures and hydraulic fractures are modeled as pairs of faces elements attached to solid elements in opposing sides of the fracture. They are both created by duplicating the face element connecting two adjacent solid elements and making appropriate adjustments to the topological maps between nodes, edges, faces, and elements. The only difference between them is when the topological changes are applied: natural fractures are generated in the initialization of a model whereas hydraulic fractures are generated during the simulation.

In the initial state of a simulation, the natural fractures are usually "closed", that is, the fluid pressure in the fracture is lower than the closing stress on the fracture and therefore the two "walls" of the fracture are in contact. We use a penalty-based contact model, which is an extension of the 2D contact model presented in Fu et al. (2013), to calculate the contact stress, including normal and tangential components, between the walls. Since the contact stresses and the fluid pressure in the fracture act jointly to balance the stress in the solid elements next to the fracture, the normal contact stress is essentially the effective stress on the fracture. The maximum allowed shear contact stress on each pair of contacting faces is determined by the Coulomb criterion parameterized with a coefficient of friction and a cohesion.

A closed fracture has a negative geometrical aperture because the two opposing walls need to geometrically "penetrate" into each other to invoke the penalty-based contact model. However, it is known that closed fractures are hydraulically conductive due to mismatches of asperities (Cook, 1992). We relate the aperture of closed fractures (w) to the normal contact stress (σ'_n) through the Barton-Bandis model (Bandis et al., 1983; Barton and Bandis, 1986) as

$$w = \frac{a}{b(1 + b\sigma'_n)} \tag{1}$$

Since the two parameters in the Barton-Bandis model, a and b, do not have straightforward physical interpretations, we re-parameterize the model with a set of three parameters, the aperture at zero effective stress w_0, a reference effective stress σ'_{ref}, and the aperture w_{ref} at this reference effective stress (Guo et al., 2016). The relationship between these two sets of parameters are

$$b = \frac{w_0 - w_{ref}}{\sigma'_{ref} w_{ref}} \tag{2}$$

$$a = bw_0 \tag{3}$$

All the simulations in this work use $w_0 = 0.1$ mm, $w_{ref} = 0.2$ mm and $\sigma'_{ref} = 5$ MPa. As the fluid pressure in a closed fracture increases, the effective normal stress (i.e. the normal component of the contact stress) reduces as a result of smaller geometrical penetration between the two walls. Eventually, the contact vanishes and the fracture "opens", resulting in the fluid pressure alone balances the stress in the rock body.

Verification of MVCCT near stress contrast

The original VCCT formulation assumes zero traction on the fracture surface (Kruger, 2014). Considering that hydraulic fracturing is driven by high fluid pressure exerted on the fracture surface, a modified virtual crack closure technique (MVCCT) is required to calculate the energy release rate under this condition. The main modification is the inclusion of nodal forces resulting from the integration of the external tractions (i.e, fluid pressure in this study) on the crack surface, besides the original volume integral on the divergence of the stress tensor (Raju, 1987; Settgast et al., 2017). Both VCCT and MVCCT rely on a self-similarity assumption, that is, the near-tip region deformation of a fracture does not substantially change after a crack extension (by one element-length). When the tip of a fracture propagating perpendicularly to the bedding plane direction is near or at the interface between two layers with distinct stresses, which is the main condition investigated in the current work, this similarity assumption could become problematic. A high-fidelity hydraulic fracture code based on MVCCT should be able to demonstrate accurate prediction of fracture height under complex stress profile. Here we verify the applicability of MVCCT to the concerned configuration through a comparison with an analytical solution and a method that computes the energy release directly (termed "direct energy" method hereafter).

For a crack in an elastic body subject to a load, the energy release rate is defined as the decrease in the potential energy of the whole system associated with an extension of the crack by a unit area (Banks-Sills, 1991). The potential energy includes both elastic strain energy and the potential energy of the applied loading. The direct energy method calculates the energy release rate directly based on this definition. We consider two states of the system: The reference state is the current state, including the current fracture configuration and the external loading. The virtual extension state is where we extend the fracture from the tip on which we are evaluating the energy release rate, by one element-length. We calculate the total potential energies at these two states by summations over all the finite elements. The ratio between the difference (between the two states) in the potential energy and the difference in the area of the fracture (i.e. the virtual extension area), is calculated as the energy release rate. This procedure is a straight application of the definition, so it produces consistent and reliable solutions for benchmarking purposes.

A classic equilibrium-fracture-height model, i.e., a vertical fracture under the plane-strain condition subjected to uniform internal pressure p and vertically-varying horizontal in-situ stresses, is used to validate the applicability of MVCCT when the fracture is near and crosses a stress barrier. The conceptual model is illustrated in Figure 1, where the fracture spans three horizontal layers. The stress contrast $\Delta\sigma$ between the middle layer and the upper layer and that between the middle and lower layers is the same, establishing symmetry against the mid-height horizontal plane. The analytical solution of the stress intensity factor at each tip of fracture, when the fracture extends by length x into the upper and lower layers, is given by Simonson (1977) as

$$K_I = (p - \sigma_h)\sqrt{\pi h} + 2\Delta\sigma\sqrt{\frac{h}{\pi}}\sin^{-1}(\frac{h_0}{h}) \tag{4}$$

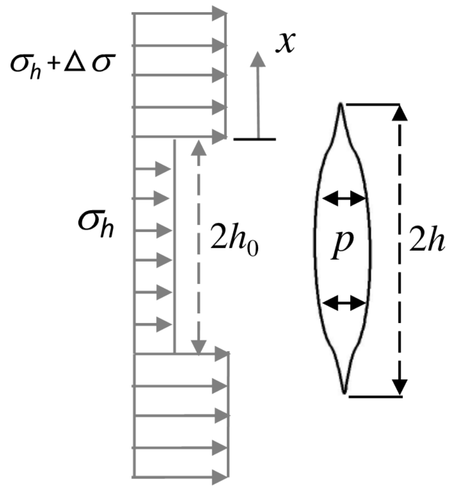

Figure 1— Configuration of a hydraulic fracture growing into higher-stress formations with uniform fluid pressure inside. Only the upper half of the model is analyzed due to symmetry. A local 1D coordinate system is established with its origin placed at the stress contrast interface. The fracture tip location x is the penetration depth into the higher-stress layer.

In the validation simulation, the formation toughness is K_{Ic} = 1.0 MPa•m$^{0.5}$, middle layer thickness is $2h_0$ = 20 m, stress difference at the interfaces is $\Delta\sigma$= 2 MPa, and hydraulic fracture center is assumed to be 10 m below the stress barrier. Figure 2 shows the comparison of net fracturing pressure (p-σ_h) of a fracture extending from the midpoint of a 20 m thick, lower-stress layer into an infinite-thickness, higher-stress (by 2 MPa) layer. The same 1D coordinate system x, established in Figure 1with its origin placed at the stress barrier interface, is used as the horizontal axis. Note that a negative x value means the fracture is within the middle layer and its distance to the stress contrast interface is $–x$. The results based on the MVCCT method are compared with both analytical solution and solutions from the direct energy method. Note that neither of these numerical methods directly calculates the propagation depth or the fracture length. We use an iterative procedure to derive the fluid pressure that yields K_I = K_{Ic} for the assumed fracture length. The results show that the net pressure decreases with the increase of fracture length when the fracture is within the middle layer but propagating toward the stress contrast interface. Once the fracture propagates into the higher-stress layer, the fluid pressure first sharply increases and then the rate of increase becomes rather modest. Even after the fracture is more than 100 m into the higher-stress layer, which is 10 times the half-height of the middle layer, the required pressure to continue propagation is still lower than the closure stress in this layer. The three methods provide nearly identical solutions to the problem, confirming the applicability of MVCCT to the problem of interest in the current study.

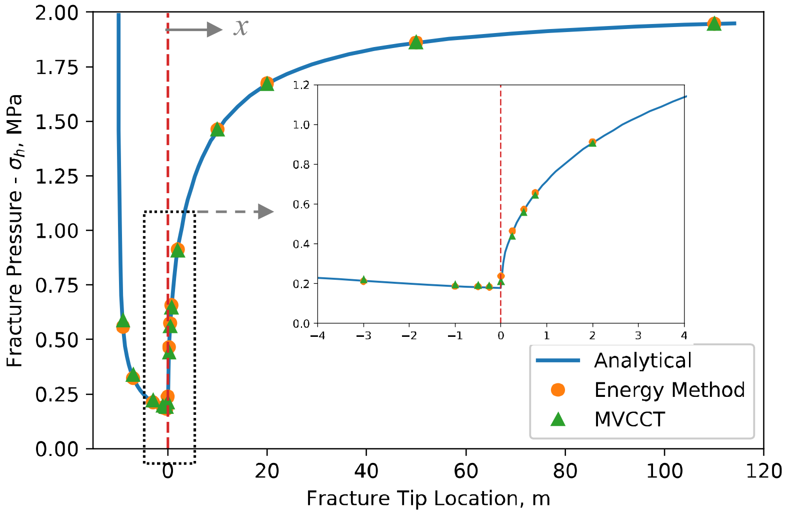

Figure 2—Comparison of net fracturing pressure of a fracture extending from the midpoint of a 20 m thick, lower-stress layer into an infinite-thickness, higher-stress (by 2 MPa) layer. Red dashed line indicates the interface of the stress barrier. The coordinate system *x*, established in Figure 1 with its origin placed at the stress barrier interface, is used as the horizontal axis.

Baseline Simulation: Hydraulic/Natural Fracture Interaction at Stress Barrier

In the subsequent sections, we narrow our focus on the how a hydraulic fracture's height growth into and beyond a stress barrier is influenced by natural fractures. The mechanism discussed here is associated with the alteration of in situ stress field caused by the shear activation of natural fractures.

We consider a vertical hydraulic fracture that is bounded by a hard barrier in its bottom and propagates upward to a strong stress barrier, that is, a relatively thin layer with S_{hmin} higher than the rest of the pay zone. Two natural fractures vertically crossing through the stress barrier but not spanning the entire height of the pay zone are considered. Figure 3 shows a plan view and a side view of the simulation model where two natural fractures, named NF1 and NF2, intersect the trajectory plane of the hydraulic fracture at an angle $\theta = 45°$. The coefficient of friction is assumed to be 0.65 in natural fractures while cohesion is assumed to be zero. The two natural fractures are 200 m away from each other along the hydraulic fracture plane. The hydraulic fracture, perforated in the lower pay zone and horizontally located in the middle between the two natural fractures, is projected to intersect the middle length of NF1, and intersect NF2 near one of the tips. The stress barrier layer, highlighted in yellow in Figure 3 (b), is 13 m thick and located within a pay zone of 90 m thickness that is assumed to be strictly bounded by the upper and lower formations. The minimum in-situ stress S_{hmin} is 11 MPa in the pay zones except that it is 2 MPa (290 psi) greater in the stress barrier layer. The horizontal differential stress between S_{Hmax} and S_{hmin} is 3 MPa in all layers. We consider injection of slickwater with 1 cP viscosity at a constant rate of 38 barrel per minute (BPM) or, equivalently, 0.1 m^3/s.

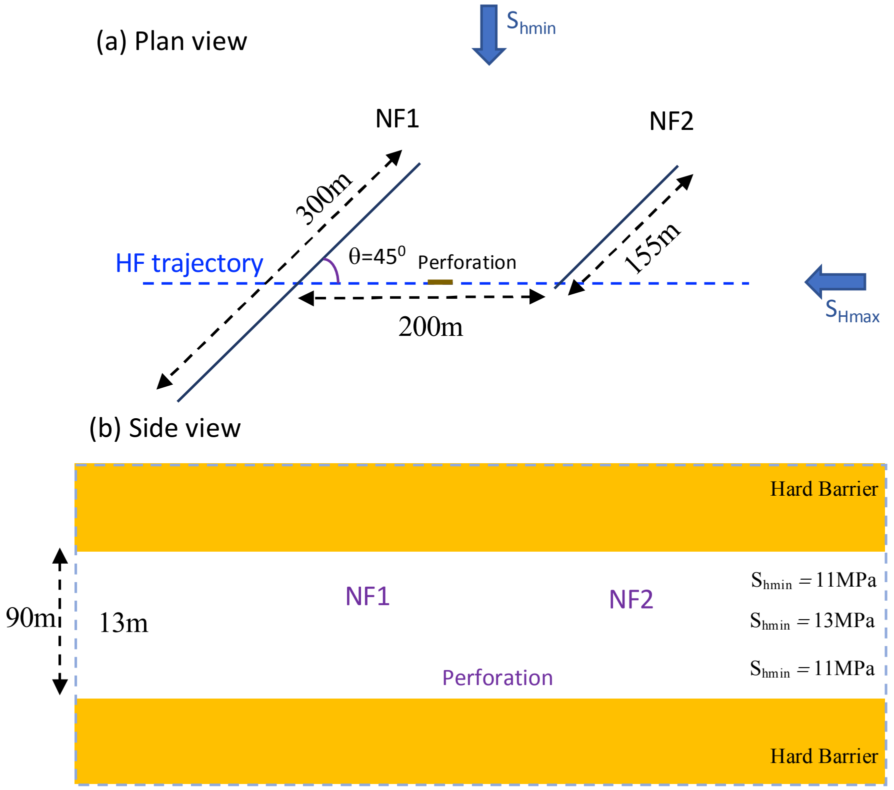

Figure 3—The baseline model for hydraulic/natural fracture interaction near a stress barrier. (a) Plan view of a potential planar hydraulic fracture intersecting two natural fractures at different positions. (b) Side view with highlighted location of the stress barrier that natural fractures cross. The fracture trajectory plane is made semi-transparent to allow viewing the natural fractures on the other side of the plane.

Figure 4 shows the evolution of injection pressure near the injection point with pumping time. The 3D fracture propagation model clearly captures several important stages of the stimulation: the initially high pressure before significant fracture growth (point *a*), the pressure buildup as the fracture propagates (around point *b*), the peak pressure associated with the breakthrough of the stress barrier (at point *c*), and the subsequent pressure decay (after point *d*). At early time, the hydraulic fracture extends laterally within the lower part of the pay zone. The corresponding injection pressure increases gradually with the extension of fracture length, resembling a classical Perkins-Kern-Nordgren (PKN) model. With pressure buildup, the hydraulic fracture eventually breaks through the stress barrier and starts propagating in the upper half of pay zone. As a result of the greater overall fracture height, the pressure significantly decreases after the breakthrough.

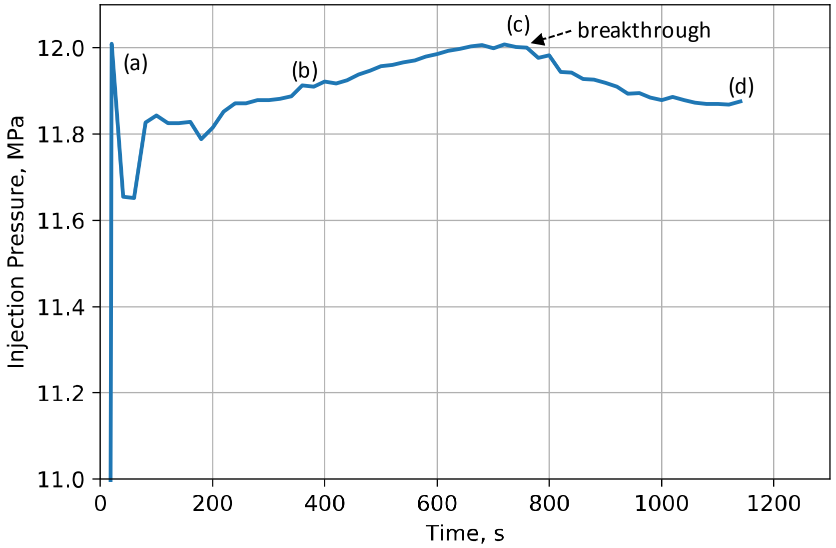

Figure 4— Evolution of injection pressure near injection point with pumping time. Times (a) through (d) correspond to the snapshots rendered in Figure 5.

Figure 5 shows the status of the system at four representative times marked in Figure 4, with fracture pressure and aperture distributions displayed from different views, respectively, on all the fractures. The hydraulic fracture is observed to first break through the stress barrier where it intersects NF2 near one of the tips of NF2. Subsequently, the fracture starts to propagate primarily in the upper pay zone, along with the continuous opening of the remainder of the stress barrier.

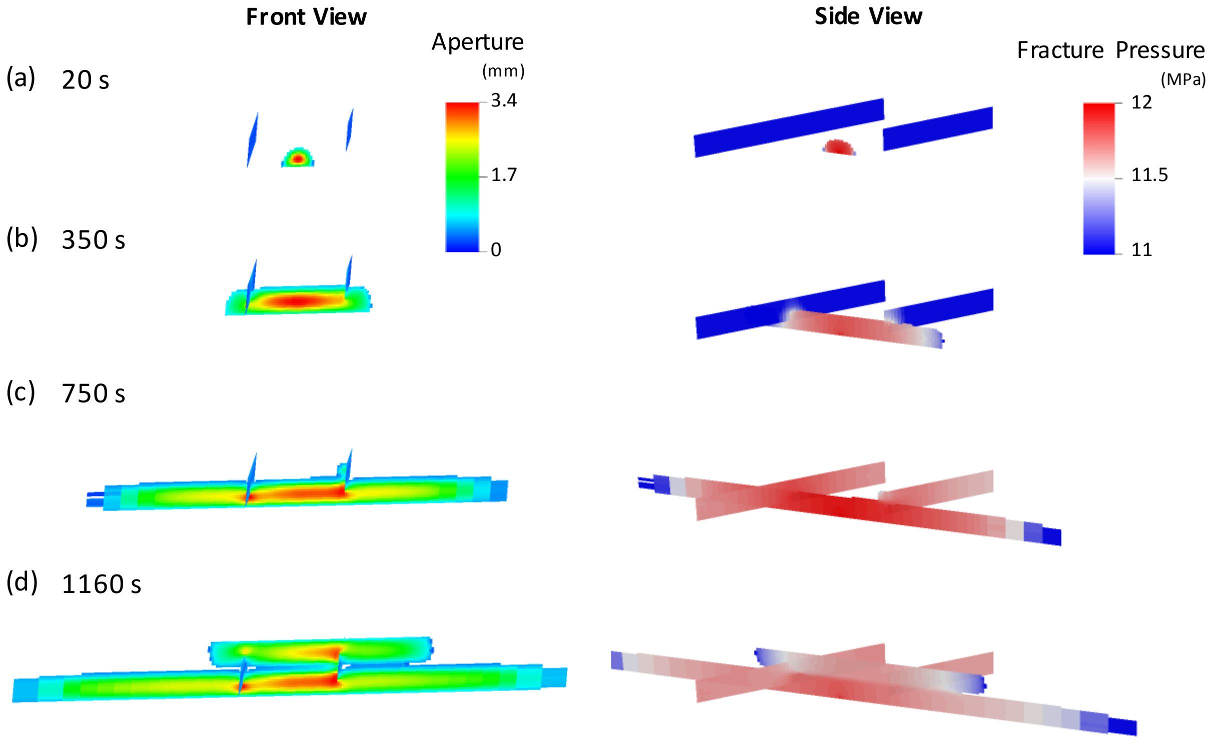

Figure 5—Configuration of intersection between hydraulic fracture and natural fractures with fracture aperture and pressure distributions at different times (a) through (d) corresponding to those referred to in Figure 4.

Figure 6 shows the time evolution of the hydraulic fracture and its interaction with the stress barrier and natural fractures. The color on the hydraulic fracture surface denotes the time when the fracture reached that location, which we refer to as the time of fracturing (TOF). A combined analysis of Figures 5 and 6 shows that at early times, the hydraulic fracture is vertically contained by the stress barrier. Later, the fracture propagates into the upper half of the pay zone through the passage created by the early breakthrough on the left side of NF2 (see Figure 6 (a)). One interesting phenomenon can be observed from the close-up view in Figure 6 (b) is the breakthrough location near natural fractures. There are two sides for each natural fracture and hydraulic fracture intersects NF1 from NF1's right side and NF2 from NF2's left side. However, the hydraulic fracture only breaks through the stress barrier from the left side of NF2. In contrast, the other three sides (both sides of NF1 and right side of NF2) cannot be broken within the simulation time (i.e., white holes in Figure 6 (b)), even after other parts of the stress barrier have been broken. It is evident that natural fracture alters the propagation pattern of the hydraulic fracture. To compare breakthrough time along the stress barrier, we choose five vertical lines that are 10 m, 30 m, 60 m, 100 m and 130 m away from the left side of NF2. Figure 6 (c) plots the time of fracturing along each line, with the correspondence between Figure (b) and (c) established by the colors of the lines in (b) and those of the curves in (c). It is observed that only along the blue line, the one closes to the fracture intersection, the fracturing time increases monotonically, which means fracturing takes place in the order of the lower pay zone, the stress barrier, and the upper pay zone. In other locations marked by the other four lines, the fracture propagates into the upper pay zone first and then breaks the stress barrier. It means, the fracture goes upward through a small segment of the broken barrier near the intersection with NF2 and then extends laterally, which "drags" the breakthrough of stress barrier below it. These mechanisms are further explored in subsequent sections.

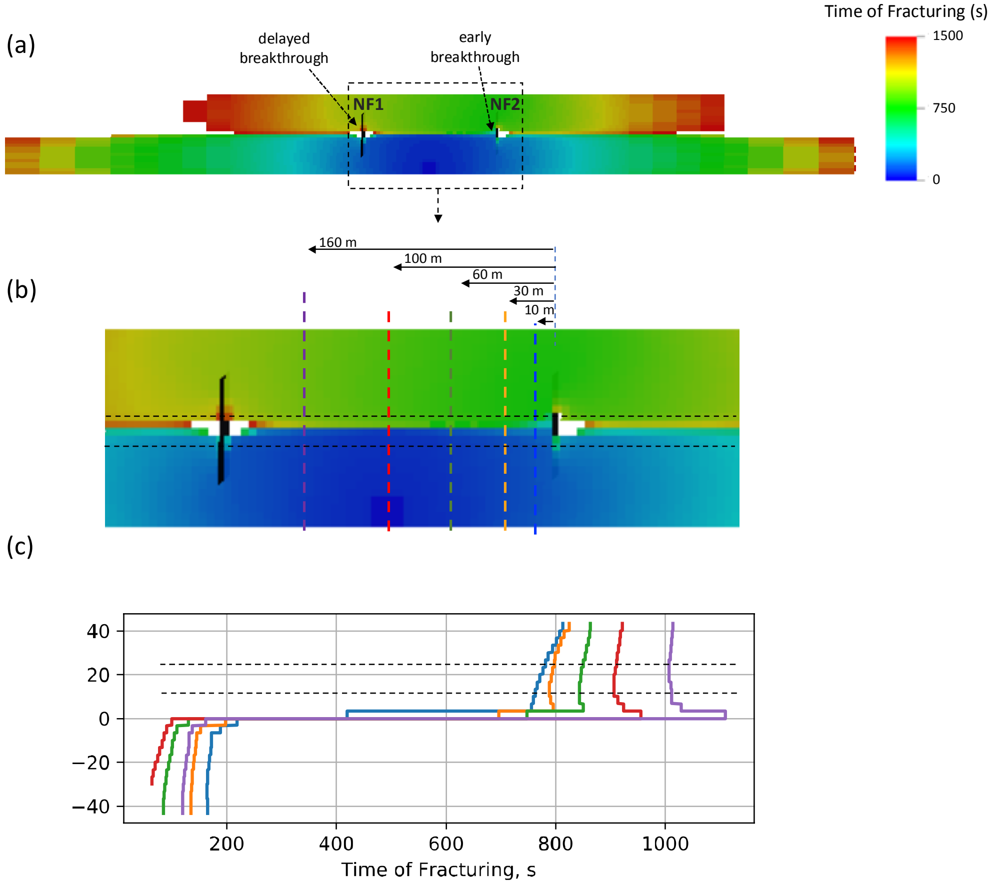

Figure 6— Distribution of time of fracturing along the hydraulic fracture, indicating the time at which that portion of the fracture was opened. Two horizontal black dashed lines in the zoomed-in view (b) mark the location of stress barrier. The colored dash lines mark vertical lines with different distance to NF2. The time of fracturing along these vertical lines is shown in (c), with correspondence between the lines in (b) and the curves in (c) established by colors.

Contributing Mechanism I: Stress Barrier Weakened by Fracture Slipping

Stress perturbation on natural fractures can be induced by both approaching hydraulic fractures and slipping natural fractures as a result of pressure interference after their intersection. Both mechanisms are naturally reflected by our fully coupled models. In this section, we focus on how the slipping along a natural fracture oblique to the principal stress direction alters the surrounding stress field after fracture intersection and thereby weakens or strengthens the stress barrier at different locations along the natural fracture. We also investigate how various factors affect such weakening and strengthening.

Our focus is the deformation and stress perturbation associated with the shear activation of a single natural fracture oriented at a certain angle with respect to the maximum in-situ stress direction. Figure 7 shows the influence of a single fracture's slip upon the displacements field of the surrounding rock. This vertical fracture is 300 m long, 50 m high, and oriented at 45° to the horizontal principal stress directions. The two horizontal principal stress components are S_{hmin} = 11 MPa and S_{Hmax} = 14 MPa, respectively. The coefficient of friction is assumed to be 0.65 in the natural fractures while cohesion is assumed to be zero, the same as those in the baseline simulation in the previous section. To demonstrate how the elevated pore pressure initiates the slip on the natural fracture plane, we apply a constant internal pressure p = 12.5 MPa along the lower half of the vertical line in the middle (laterally) of the fracture to mimic the intersection of a hydraulic fracture from which fracturing fluid flows into natural fracture. Along a fracture, when the shear stress exceeds the product of normal contact stress and the coefficient of friction, the shear slip takes place. When the system reaches an equilibrium, in which the entire fracture reaches the applied pressure (i.e., 12.5 MPa), the fracture has nearly zero normal contact stress and therefore slipping occurs over the full length. The displacement field on a horizontal plane cutting the natural fracture at the mid-height is shown in Figure 7. The solid body moves in opposite directions at the two sides of the fracture, expected to result in a significant alteration to the in-situ stress field.

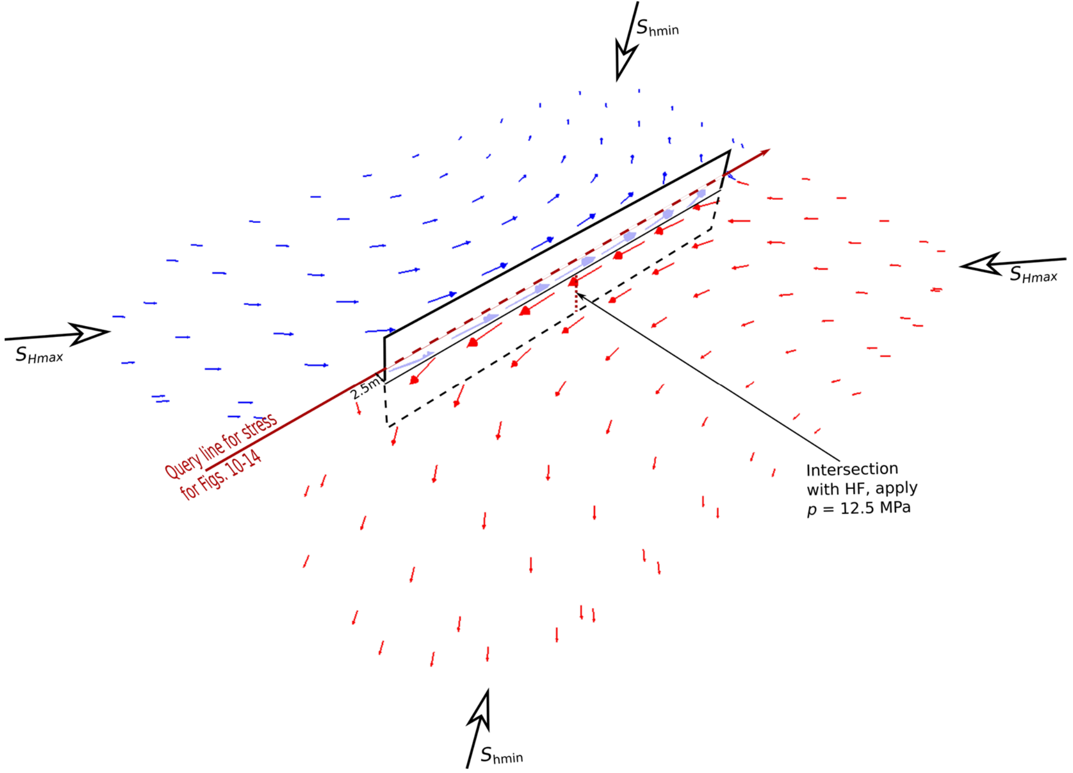

Figure 7—Influence of a single fracture's slip upon displacements of the surrounding rock when the fracture is oriented at 45° to the principal in-situ stress. The arrows depict the displacement field of the medium on a horizontal plane cutting through the fracture at mid-height. The location of the hypothetical intersection with a hydraulic fracture is marked on the plane, where a pressure boundary of *p* = 12.5 MPa is applied. The dark red line on this plane at 2.5 m from the fracture is the path of interest along which the stresses and other quantities are queried as shown in Figures 10--14.

Figure 8 displays a side view of the pressure propagation process within the natural fracture from its center to the two tips, as well as the resultant perturbation to the stress component in the direction of the original minimum horizontal stress (ΔS_{hmin}) on a horizontal plane that cuts the natural fracture at its mid-height (i.e., only the upper half is shown). Although strictly speaking, the principal stresses have rotated near the fracture plane as a result of the slipping, we refer to the change of "stress component in the direction of the original minimum horizontal stress" as the change of S_{hmin} for the sake of conciseness in the subsequent text. Note that the fracture field on the lower half of the natural fracture is blocked by the horizontal plane. Figure 9 shows the plan view of the influence of slip upon the stress perturbation. As the in-situ stress is the single most important factor affecting the trajectory of a hydraulic fracture, these plots indicate the impact of the natural fracture upon an intersected hydraulic fracture's ability to continue propagating. Regions with increased compression (blue in Figure 9) will tend to inhibit fracture propagation, while regions of increased tension (red in Figure 9) is easier for a hydraulic fracture to propagate through. As shown in Figure 9, the induced stress distribution is antisymmetric with respect to the fracture center. Along the majority of the fracture's length, slipping causes additional compression to S_{hmin} (or more strictly, the stress component in the direction of original S_{hmin}). These results indicate that a hydraulic fracture intersecting the natural fracture at its center will experience increased compression. This explains the forming the three "holes" in Figure 6 (b), i.e. induced compression preventing fracture from developing there. On the other hand, on one side near the tips of activated/slipped portion of fracture, tensile stress is induced, which indicates a chance that a hydraulic fracture intersecting a natural fracture at the tip could experience a weakened stress barrier at the tensile side and thus more readily have the potential to break through a stress barrier, if present. This stress distribution shown in Figure 9 explains why the breakthrough only occurs at one of the four intersections, i.e, both sides of NF1 and NF2 in Figure 3 (a). Consequently, we expect that natural fractures can both encourage and inhibit the progress of hydraulic fractures propagating through stress barriers, depending upon the relative locations between the intersecting fractures.

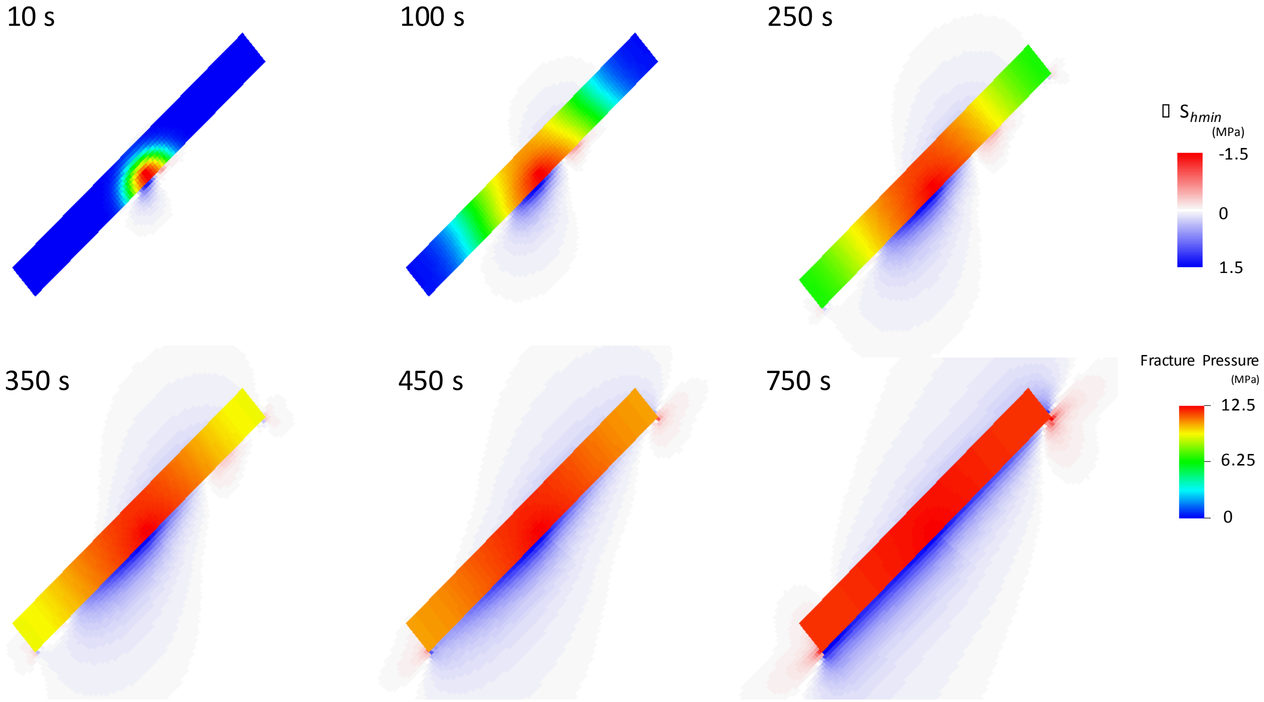

Figure 8—Side view of pressure propagation within natural fracture from its center to two tips and the induced stress perturbation. A constant pressure source along the lower central line of the fracture is assumed to mimic hydraulic fracture intersection. The stress perturbation (ΔS_{hmin}) plotted is on a horizontal plane cutting the fracture at its mid-height.

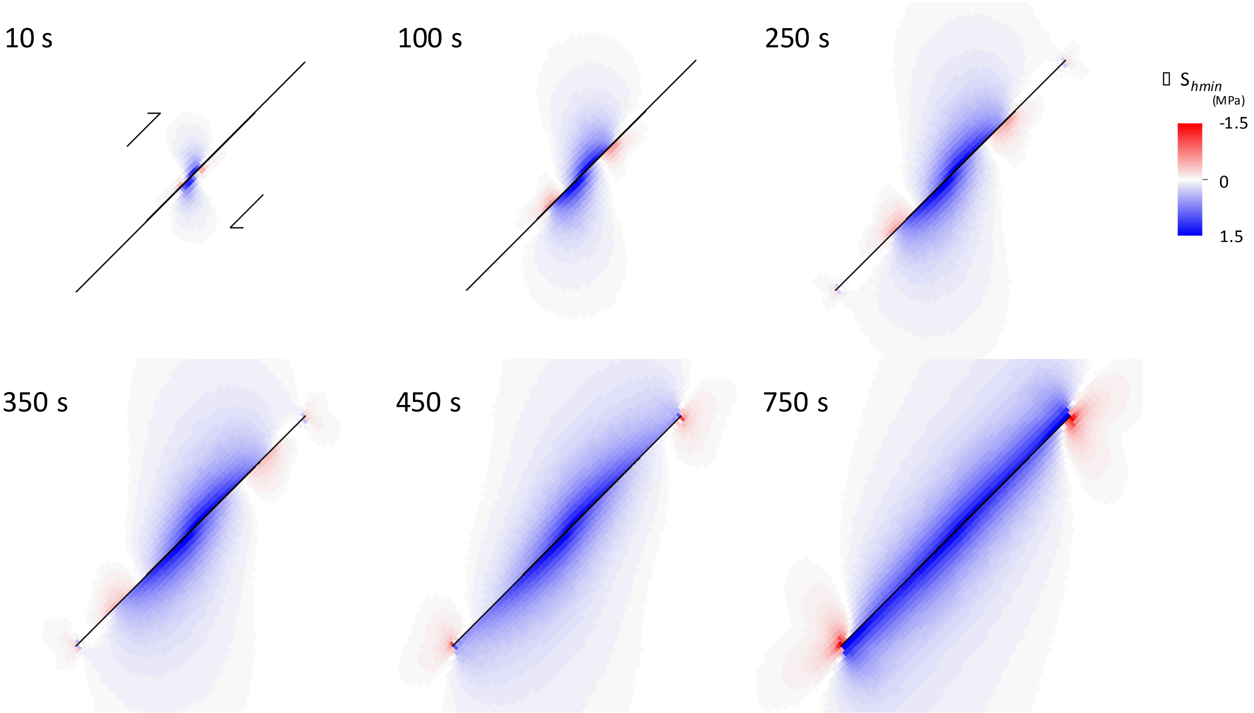

Figure 9— Plan view of the influence of slip on the minimum in-situ stress component in the surrounding rock as a result of pressure propagation along the natural fracture. The color represents the induced stress on a horizontal plane cutting through the fracture at mid-height. Blue indicates an increase in compression and red indicates an increase in tension.

To quantitatively study the slipping fracture's alteration of the surrounding stress, Figure 10 plots the evolution of pressure within the natural fracture, the resultant shear displacement (which is half of the relative slipping due to symmetry), and S_{hmin} increment along a path that is 2.5 m from the natural fracture plane, as denoted by the dark red query line in Figure 7. A simple analytical calculation on the same phenomenon is performed by Zoback et al. (2012). In Figure 10, six colored curves corresponding to various times illustrate the time evolution. As time goes on and pressure spreads out from mid-point of the fracture to the tips, the slippage front moves accordingly, accompanied by the increase of shear displacement and S_{hmin} perturbation. A modest amount of tensile increment develops around one slip front of the fracture, whereas only compression develops around the other slip front. Two observations are worth noting. First, the fluid pressure at the slip front is lower than that based on an average calculation for the fracture as a whole. The theoretical value of pressure required for the fracture to slip as a whole is 12.5 – 1.5/0.65 = 10.2 MPa, where 12.5 MPa is the average total normal stress on the fracture, 1.5 MPa is the original shear stress on the fracture plane, and 0.65 is the coefficient of friction. The three vertical dash lines mark the location of the 10.2 MPa at three times and slipping at the corresponding times is ahead of these marked locations. This is because the slipping in the middle portion of the fracture causes stress redistribution and thereby increases the shear stress on the rest of the fracture. The second observation is that significant stress perturbation occurs near the ends of the fracture before the arrival of the slip front, due to tip-region singularity. After the slip front arrives at the fracture tip (t > 450 s), the tensile stress near the tip continues to increase as a larger portion of the fracture experiences higher fluid pressure and undergoes more slipping.

It is worth noting that small oscillations of S_{hmin} increment are observed near the ends of the fracture before the arrival of the slip front. This oscillation is induced by the low-order penalty-based contact model we adopt for closed natural fractures, that is, only the mid-point on each element face is used to calculate the penetration depth (Fu et al., 2013). In this contact model, the normal contact stress is proportional to the penetration depth between the two opposing faces (or edges in 2D) at their centers. The resultant oscillating contact stress is analogous to the hourglass modes in under-integrated finite elements (Belytschko et al., 1984). However, the magnitude of this oscillation is trivial compared with the induced stress when the slip front arrives at the fracture tip and thus not overwhelming the main process that we investigate in the current study.

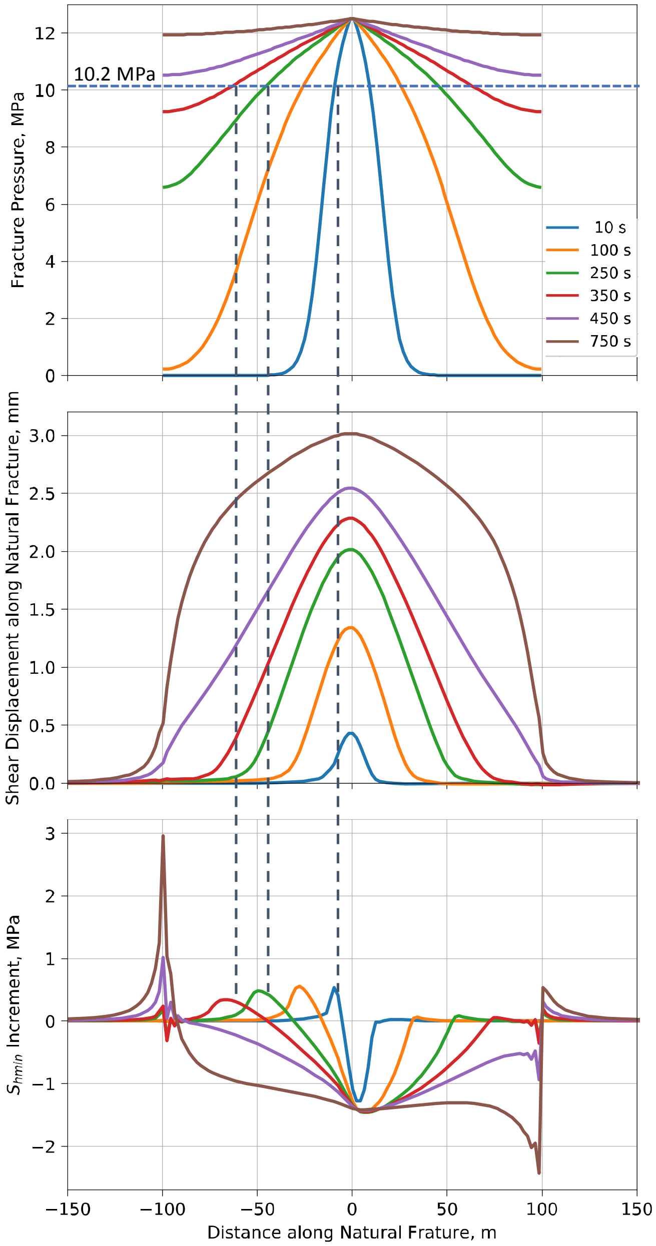

Figure 10— Evolution of pressure along the natural fracture and the resultant shear displacement and S_{hmin} increment along a path 2.5 m from the natural fracture (i.e., red query line in Figure 7).

Having identified the mechanisms of natural fracture slipping and the effect it can have upon stress perturbation, we investigate the sensitivity of the alteration of S_{hmin} to variations in the fluid pressure at the hydraulic-natural fracture intersection, the magnitude of horizontal stress difference, the orientation of the natural fracture, as well as injection fluid viscosity.

Sensitivity to intersecting pressure

Figure 4 shows that the pressure at injection has a narrow range between 11.8 MPa and 12 MPa after hydraulic fracture intersects the natural fracture. Generally, pressure loss from injection point to near the fracture tips along an open fracture is relatively small. Therefore, on the isolated natural fracture model used for the sensitivity study, we vary the value of the pressure boundary condition applied at the hypothetical intersection line with the hydraulic fracture (referred to as the intersecting /source pressure) and examine how this pressure affects the development of the induced stress around natural fracture. Note that the original average normal stress and shear stress exerted on the natural fracture are 12.5 MPa and 1.5 MPa (as S_{hmin} = 11 MPa, S_{Hmax} = 14 MPa, 45° NF, friction $\mu = 0.65$ for baseline case), respectively. Figure 11 compares the results of simulations with three levels of source pressure at an intermediate time step t = 350s and a late time step t = 750s when fracture is fully activated. Higher source pressure causes faster propagation of the pressure front and also forces more shear stress relaxation. Therefore, higher source pressure is associated with a larger S_{hmin} increment in both in magnitude and extent, and in both the tensile and compressive sides.

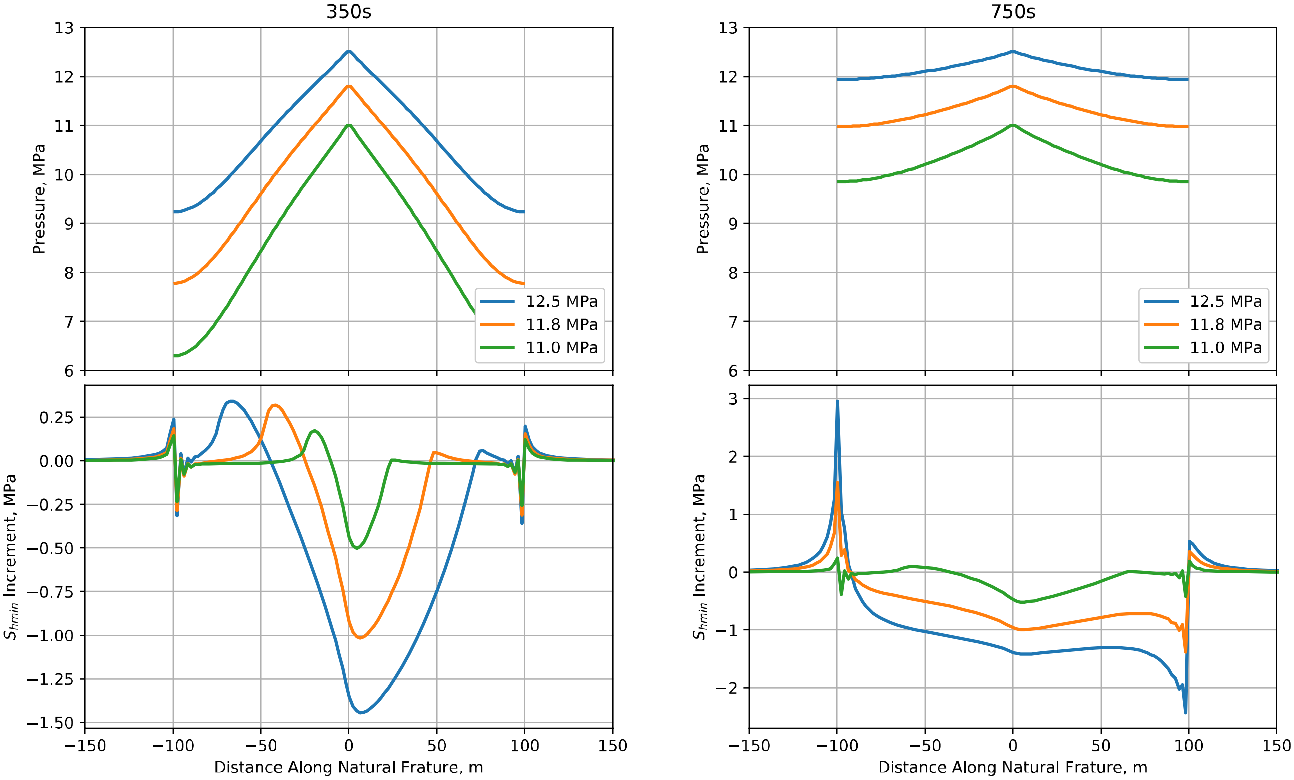

Figure 11— Sensitivity to fluid pressure in the intersection on S_{hmin} increment at different times

Sensitivity to horizontal differential stress

In the baseline model presented above, the maximum horizontal stress was $\Delta\sigma$ = 3 MPa (435 psi) over the minimum horizontal stress. One might expect that as this stress difference is reduced, the influence of the natural fractures would be lessened. Figure 12 compares S_{hmin} increment covering a range of differential stress from 1 MPa (145 psi) to 5 MPa (725 psi). It is clear that horizontal differential stress has little effect on the pressure propagation within the natural fracture as shear dilation is not considered in the model. It should be noted that under the current intersecting pressure, the natural fracture is still closed and aforementioned Barton-Bandis model is applied to update the aperture. The horizontal differential stress would impact the normal stress exerted on the natural fracture and therefore its aperture, but this impact on closed fracture is very small and not discernable in the figure. The induced stress decreases when the stress difference is reduced, as expected. Moreover, the extent of slipped fracture is larger under large stress difference, which indicates an earlier full activation of natural fracture.

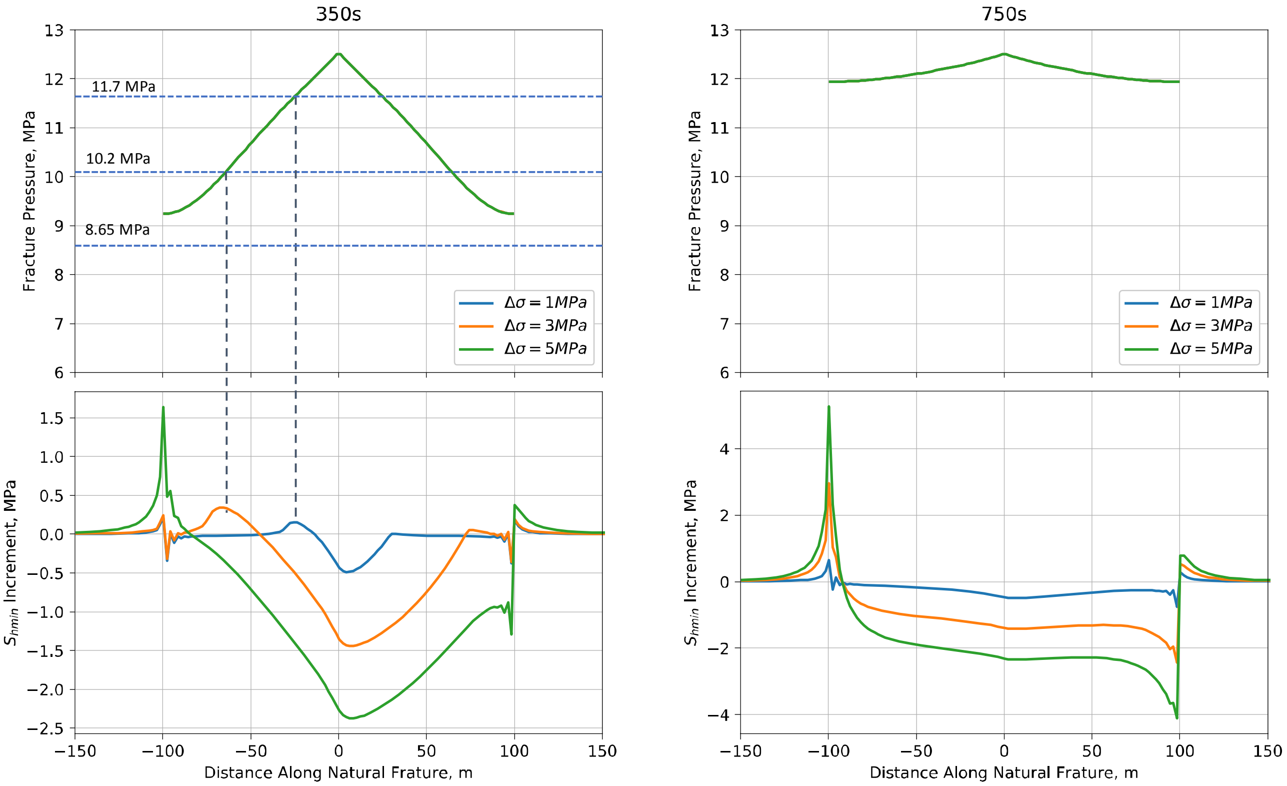

Figure 12— Sensitivity to differential stress on S_{hmin} increment at different times.

Sensitivity to natural fracture orientation

The orientations of natural fracture are often unrelated to that of the present-day stresses in a rock mass for the reasons such as regional stress regimes change through time, or the influence of paleo stresses (ancient stresses) may no longer prevail (Engelder, 1993). Thus, we examine three representative orientations to study its influence on slip-induced stress alteration. Figure 13 compares the results of simulations with varying angles between hydraulic fracture and natural fracture increasing from 30^0 to 60^0. Similar to the effects of horizontal differential stress, the orientation of natural fracture has little effect on the pressure diffusion within the natural fracture. In this scenario, the closure stress varies with the fracture orientation. When the intersecting pressure becomes larger than closure stress, the fracture would slip rapidly. To clearly see the comparison during the intermediate time, we reduce the intersecting pressure from 12.5 MPa to 11.8 MPa in this particular sensitivity study. Therefore, from the figure we observe that smaller angle (i.e., natural fracture is more parallel to hydraulic fracture and perpendicular to minimum in-situ stress) is much easier for fracture slip as the closured stress is smaller. In contrast, natural fracture with larger angle is harder to slip if the same intersecting pressure is assumed.

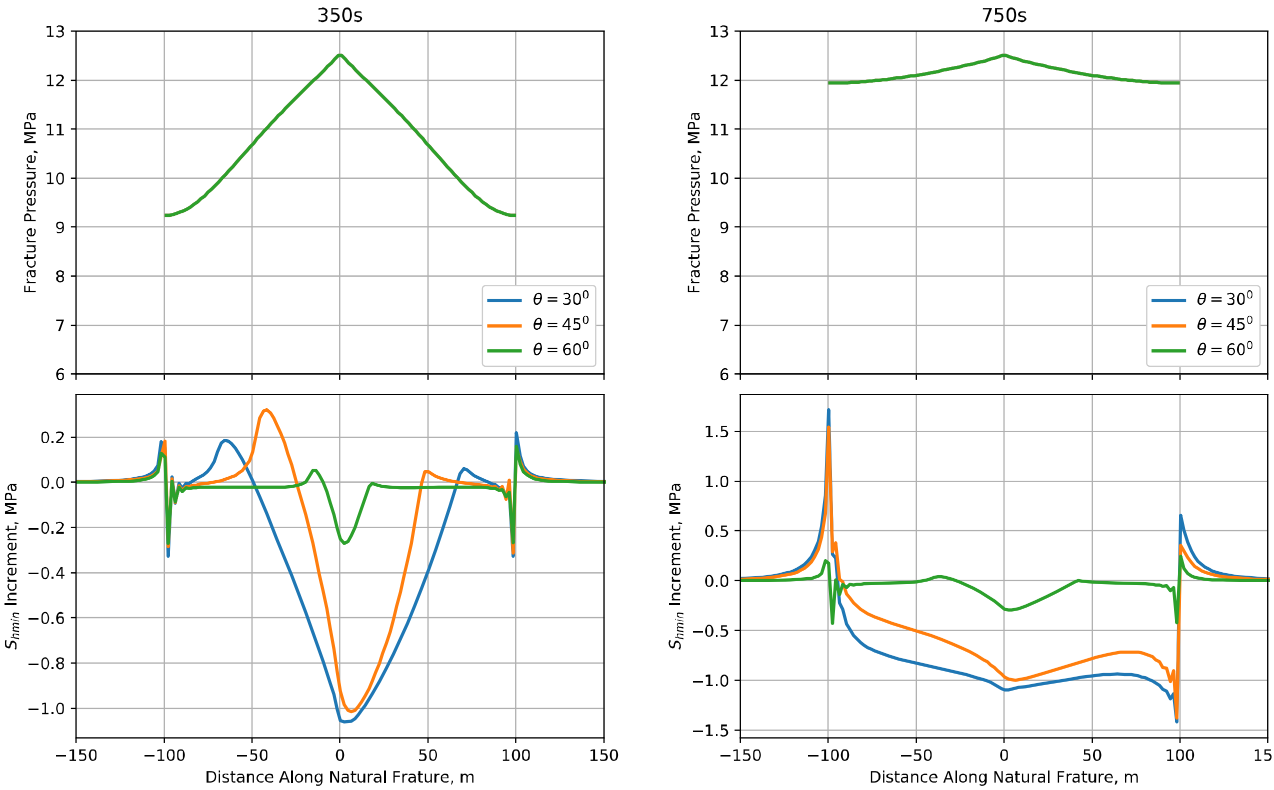

Figure 13— Sensitivity to natural fracture orientation (angle between natural fracture and hydraulic fracture) on S_{hmin} increment at different times

Sensitivity to fluid viscosity

All previous models assumed a 1 cP fracturing fluid viscosity. Previous work has confirmed for 2D geometries that hydraulic fractures are less easily diverted by natural fractures as fluid viscosity is increased (Zhang and Jeffrey, 2008; Chuprakov, 2013). Similarly, it might be expected that the slipped portion of natural fracture might be smaller with increasing fluid viscosity under the same injection volume. Figure 14 compares the results of simulations with viscosity from 1 cP to 50 cP. We observe that increasing viscosity from 1 cP to 10 cP significantly limits the pressure diffusion speed and reduces the extent of stress perturbation zone. However, the further increase from 10 cP to 50 cP results in a less impact.

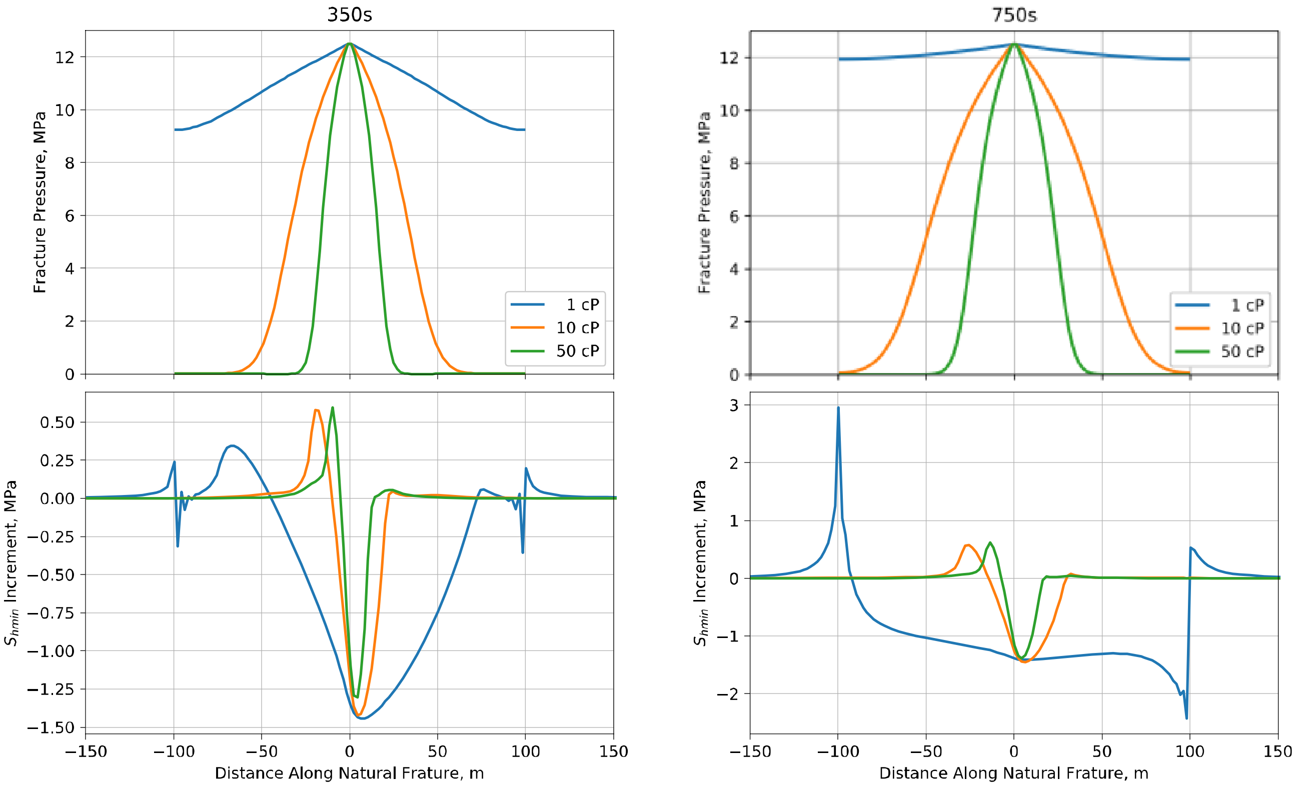

Figure 14— Sensitivity to fracturing fluid viscosity on S_{hmin} increment at different times

Contributing Mechanism II: Tip Interference between Opposing Fractures

In Figure 6, we have observed that once the hydraulic fracture breaks through the stress barrier at some weakened spots and starts to propagate in upper pay zone, the remaining unbroken stress barrier seems to become easier for hydraulic fracture to open. We hypothesize that when two fracture tips attempt to break into a stress barrier from opposing sides, the required pressure is significantly lower than the pressure required if a single fracture tip attempts to break the stress barrier. This hypothetical mechanism plays an important role in the complete opening of the remaining stress barrier, because the contributing mechanism I alone can only affect a small segment of the stress barrier. Note that our model does not consider the potential fracture offset mechanism at the intersection, which has been observed in both the field and laboratory experiments (Warpinski and Teufel, 1987; Jeffery and Settari, 1995; Fu et al., 2016). In our model, fractures propagate along inter-element faces, which does not allow the offset process, even though we do not generally pre-define fracture planes. However, this limitation does not affect the main conclusions of the current study. In the scenario where there is offset between the top and bottom parts of the fracture, it is unlikely that the two parts develop into separate hydraulic fractures that continue to propagate in parallel to each other. The most likely scenario is that the offset is relatively small that the top and bottom parts eventually converge due to the imposed shear stress upon each other when the echelon fracture segments interact mechanically (as speculated in Pollard and Aydin, 1984 based on the laboratory and field observations). In that case, the offset may affect the near-intersection configuration of the fractures but not the overall configuration in a larger length scale.

To quantitatively demonstrate this hypothesis, the classic fracture height growth model in the earlier verification section is revisited to compare the net pressure required for fracture breakthrough, under the interference between the two fracture tips taken into consideration. Figure 15 (a) shows a representative configuration extracted from the baseline model, where the fracture tip from top and bottom sides of the stress barrier interfere each other. Figure 15 (b) is a 2D modified model (based on the classic fracture height growth model) we use in this section to study the fracture tip interference that conceptually represents the cross-section indicated by the black dash line in Figure 15 (a). The color in Figure 15 (b) represents the relative magnitude of horizontal stress, deeper blue meaning stronger compression. The induced tensile stress near fracture tip can alleviate the confining stress in barrier zone and promote the propagation of each other. Two values of the stress barrier thickness h_b = 2 m and 4 m are considered. We assume that below the stress barrier a fracture already extends throughout a relatively low-stress zone with a thickness of $2h_0$ = 20 m, and the same applied to the material above the barrier. The two fractures are perfectly symmetric with respect to the central line of stress barrier zone, and they propagate in the same speed to each other.

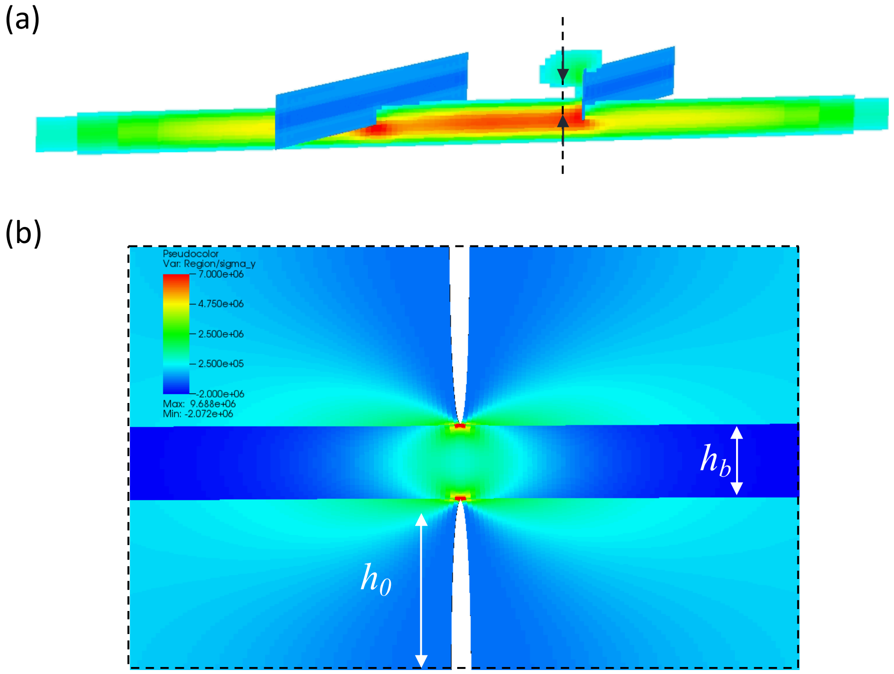

Figure 15— Configuration of fracture tip interference near a finite thickness stress barrier. (a) A 3D view of the scenario where fracture tip interference occurs. The color denotes aperture with red representing a larger aperture. At the location marked by the black dashed line, the hydraulic fracture is trying to penetrate into the stress barrier layer from above and below. (b) A modified 2D model to study the fracture tip interference at the cross-section indicated by the black dash line in (a). The color represents the relative stress magnitude (σ - σ_h) in the minimum in-situ stress direction. Positive value indicates tensile stress.

In this reduced model, an analytical solution is not available when fractures inference and stress barrier coexist, although the analytical solution of SIF for a simple two fractures inference (tip to tip) can be found in the literature (Tada et al., 2000). Therefore, the direct energy method is used, along with MVCCT, in this analysis. Verifying the applicability of MVCCT in such scenarios is important as we use MVCCT in modeling the actual propagation of hydraulic fractures as in the baseline model and in the sensitivity analyses in next section. Figure 16 shows the same plot as Figure 2 but considers two-tip interference in a finite thickness stress barrier. The analytical solution for a single fracture propagation from Figure 2 is also plotted as a reference to illustrate the effect of fracture tip interference on the fluid pressure required to propagate the fracture into/through the barrier. Note that in the opposing-tip scenario, each fracture only needs to break half of the height of the stress barrier to result in a complete breakthrough. The results show that the required fluid pressure for fracture growth is significantly lower than the reference solution and the difference increases drastically when two tips get closer. The maximum required pressure occurs approximately when each fracture penetrates into ¼ of the total barrier thickness. If we define the "net pressure" in this case to be the difference between the mean fluid pressure and the compressive stress in the lower and upper regions, namely the bases of the two opposing fractures, the tip interference causes a very significant reduction in the required net pressure, 73% and 64% for h_b = 2 m and 4 m, respectively.

This result validates the hypothesized mechanism II and also re-confirms the applicability of MVCCT for this class of problems.

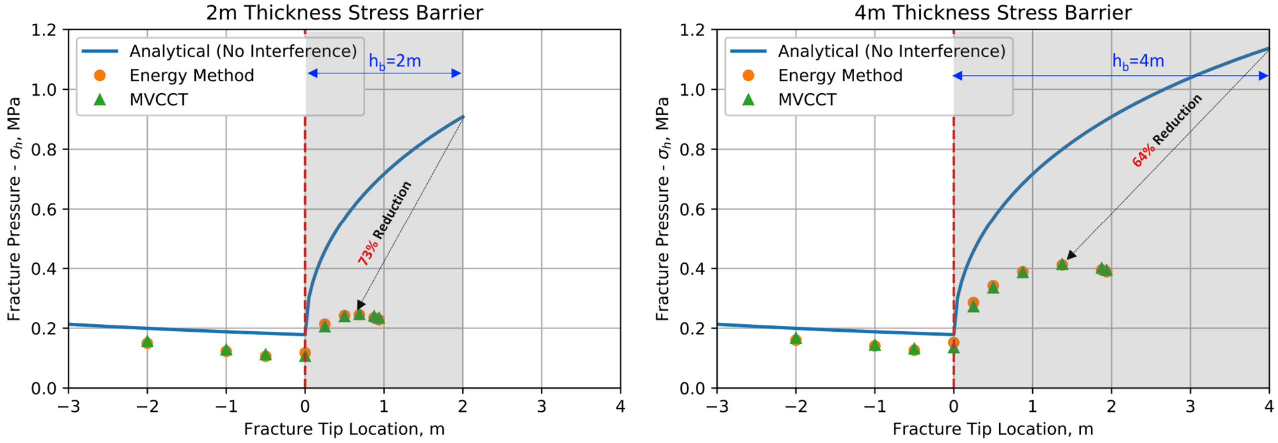

Figure 16—Variation of minimum net pressure for fracture to propagate versus fracture tip location in a finite thickness stress barrier. Red dashed line indicates the interface of stress barrier. Two thickness of stress barrier are compared. Analytical solution for a single fracture without inference is referenced.

Combined Effects of Barrier Conditions and Stimulation Parameters

The sensitivity analysis performed on a single natural fracture in the previous section has shown that the magnitude of the stress alteration caused by slipping of an oblique fracture increases with greater horizontal differential stress and greater fluid viscosity. Additionally, more viscous fluid causes higher net pressure in the original fracture zone (i.e. before breaking through the barrier), making barrier breakthrough more likely. On the other hand, stress barriers are recognized to have a significant impact on hydraulic fracture height growth (Warpinski et al., 1982a; Warpinski et al., 1982b; Nolte and Smith, 1981). It is intuitive to expect that thicker stress barriers and greater stress jump at the barrier reduce the likelihood of breakthrough. In this section, we simulate eight additional systems similar to the baseline hydraulic-natural fracture model but with different parameters, as specified by Table 1, to study the interactions between these factors. The approximate breakthrough time of each case is also listed in the table.

Case No.	Barrier Magnitude (MPa)	Barrier Thickness (m)	Differential Stress (MPa)	Fluid Viscosity (cP)	Time of Breakthrough (s)
Baseline	2	13	3	1	730
Case 1	3	13	3	1	N/A
Case 2	3	13	5	1	712
Case 3	3	13	3	10	950
Case 4	3	13	5	10	619
Case 5	2	26	3	1	N/A
Case 6	2	26	5	1	N/A
Case 7	2	26	3	10	1055
Case 8	2	26	5	10	690

Table 1—Details of eight cases modified from baseline model. “N/A” (not applicable) here means the stress barrier was not broken through at the end of the simulation.

Figure 17 plots the maps of time of fracturing for four cases with increased stress barrier magnitude (3 MPa), where the time of fracturing for the baseline case (2 MPa) is also plotted for comparison. By increasing stress barrier from 2 MPa to 3 MPa (Case 1), the hydraulic fracture is no longer able to break through the barrier. However, if a larger horizontal differential stress exists, e.g., from 3 MPa to 5 MPa (Case 2), hydraulic fracture can break through the barrier, but less fluid goes into upper pay zone compared with baseline model. The alternative way to break an increased stress barrier is to increase the viscosity of injection fluid, e.g., from 1cP to 10 cP (Case 3). Again, larger differential stress makes it easier to break through and is able to divert more injection fluid into upper pay zone, as observed from the developed fracture length in this region, as shown in Case 4.

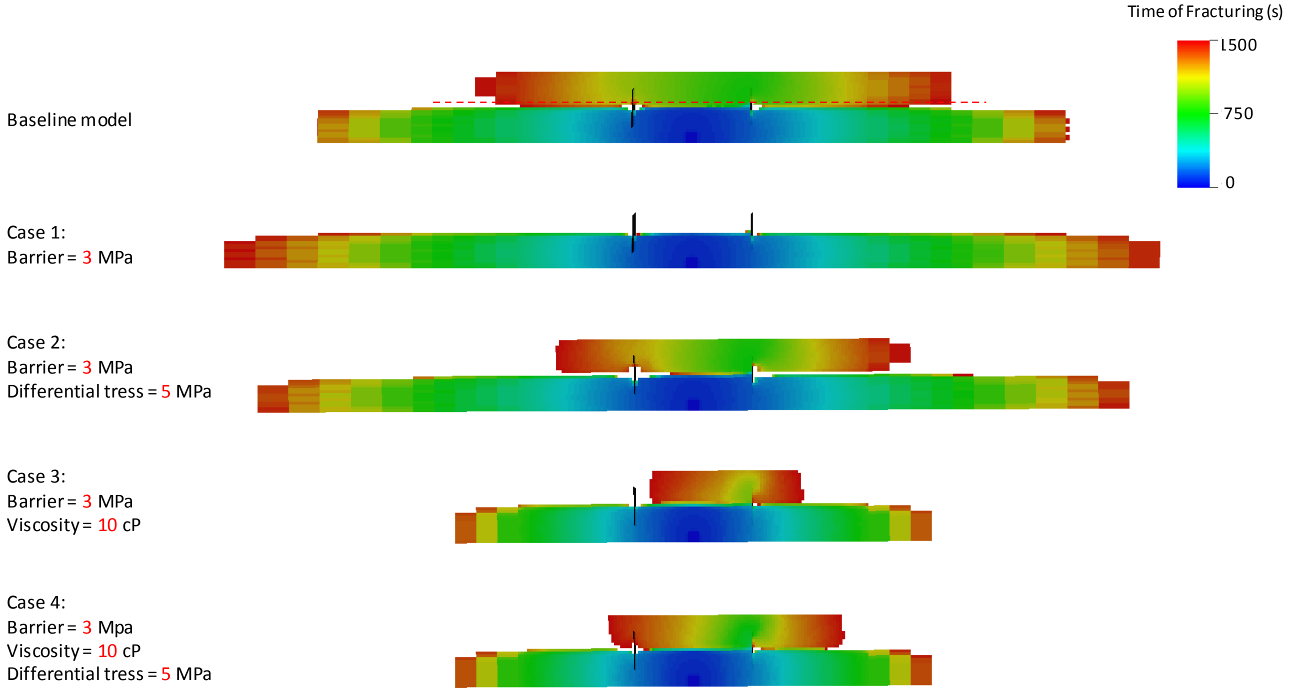

Figure 17—Variation of time of fracturing map for increased stress barrier magnitude from 2 MPa in baseline model to 3 MPa

Figure 18 plots the same map but with increased stress barrier thickness. When it increases from 13 m in baseline model to 26 m (Case 5), the fracture is fully confined within the lower pay zone, even with larger differential stress (Case 6). In contrast, increasing viscosity enables the fracture to penetrate into stress barrier zone and eventually break through the stress barrier with the help of NF2 (Case 7). Similarly, a larger differential stress reduces the barrier effect and enables more fluid into upper pay zone (Case 8).

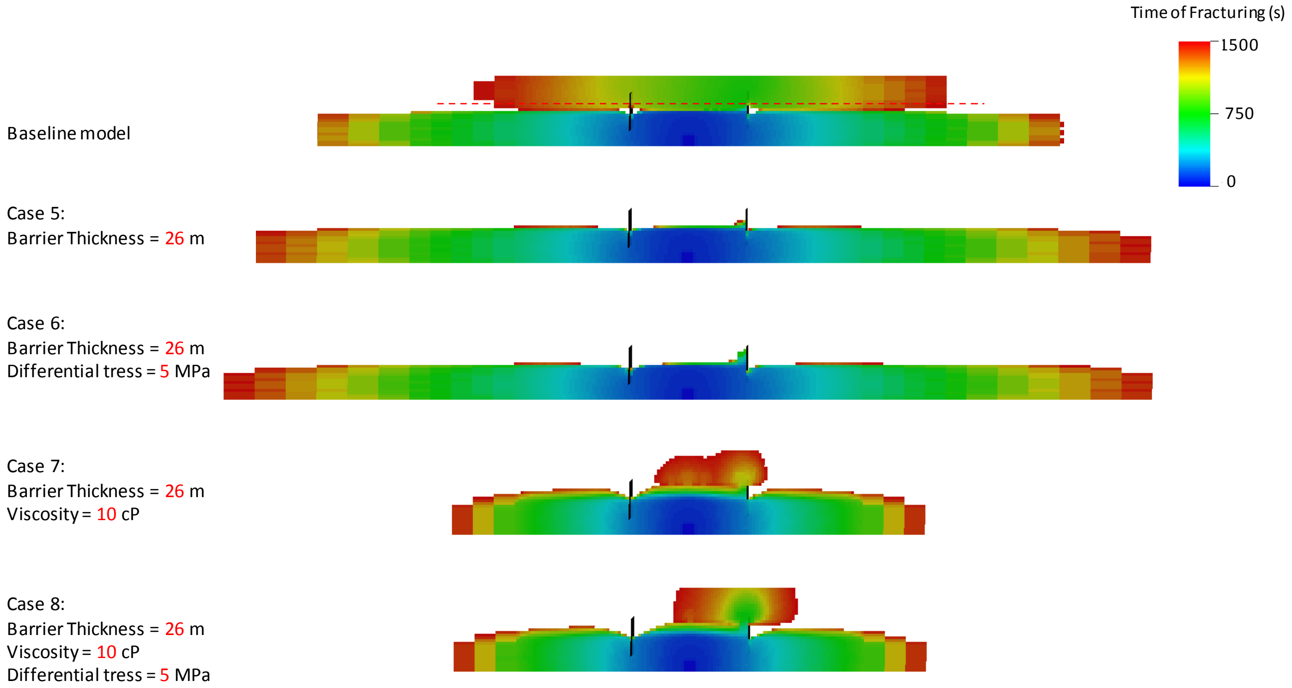

Figure 18— Variation of time of fracturing map for increased stress barrier thickness from 13 m in baseline model to 26 m

To better quantify the breakthrough time and lateral extension of hydraulic fracture in upper pay zone, Figure 19 plots the comparison of time of fracturing in the row of elements immediately above the stress barrier versus its horizontal position for these cases where breakthrough occurs. In this plot, we put origin at the center so NF1 and NF2 are at $x = -100$ m and $x = 100$ m, respectively. The baseline model shows a breakthrough time around 730s at left side of NF2 ($x < 100$ m) followed by monotonic increase of fracturing time towards both tips. Higher viscosity shows a late breakthrough of the barrier, as implied in Case 3 and Case 7. In contrast, larger differential stress results in a little bit earlier breakthrough, as implied in Case 2, Case 4 and Case 8. One interesting observation is on the right side of NF2 ($x > 100$ m) the increase is not monotonic for these cases with a larger stress barrier contrast. This indicates that fracture front is not directly propagating to the right side. Instead, it bypasses this compressed area from the above region of NF2 and then propagate back into the right side of NF2. This bypass mechanism has been detailed analyzed in (Fu et al., 2015). Another observation worthy to point out is that although it takes a longer time, a higher viscosity can directly break through the stress barrier near the injection area without the help of natural fracture, as demonstrated by a second local bottom at $x = 0$ m for Case 7. Comparison of Case 7 and Case 8 provides another insight that if the breakthrough at NF2 occurs at an earlier time, the second direct breakthrough would not happen as there is no enough time for pressure buildup near the injection area.

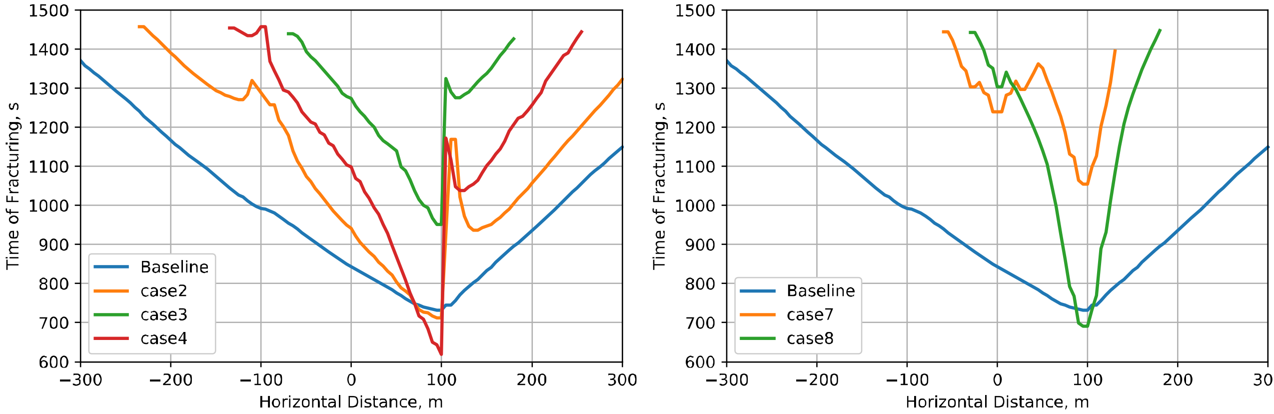

Figure 19— Plot of time of fracturing in the line of computational cells immediately above the stress barrier (red dash line in Figure 17) for variable barrier magnitude and thickness.

Conclusions

A fully coupled, 3D hydraulic fracture simulation code is utilized to investigate the combined interaction of a hydraulic fracture with natural fractures and stress barriers. A new process, through which a hydraulic fracture, with the aid of a natural fracture, can break through a stress barrier layer that would otherwise contains the hydraulic fracture's height growth, is investigated. Two significant mechanisms contribute to this process. The first mechanism is the stress perturbation due to slip of a favorably placed and oriented natural fracture. It is well known that a natural fracture oblique to principal stress directions experiences slipping when it is pressurized by the fluid from an intersecting hydraulic fracture. Such slipping can induce both increases and decreases of normal stress in the original minimum horizontal stress direction, toward the center and tip of the natural fracture, respectively. If the intersection happens to be near one of the tips of the natural fracture, the slip-induced stress alteration can weaken the stress barrier locally and allow the hydraulic fracture to propagate through. Although its occurrence seems to depend on the chance that the hydraulic fracture happens to intersect the natural fracture at a specific location, in a real stimulation this is in fact very likely to take place, given the numerous natural fractures in typical shale formations. The second mechanism is related to the interference between fractures opposing each other from the top and bottom sides of the stress barrier. A quantitative analysis finds that the fluid pressure required by such an opposing-fracture configuration to completely penetrate a stress barrier (from above and below simultaneously) is much lower than that required by a fracture penetrating from one side (from below only). The first mechanism facilitates barrier breakthrough over a small segment of the barrier layer. However, this limited breakthrough initiates an opposing-fracture configuration that "unzips" the barrier layer in a progressive fashion over the full lateral extent of the hydraulic fracture.

Together with a previous work (Fu et al., 2015), we show that the interactions between hydraulic fractures, natural fractures, and geologic factors such as stress barriers in 3D are much more complex than in 2D. Although it is impossible for a specific study to exhaust all the possible configurations, we demonstrate the ability of a 3D, fully coupled numerical model to naturally capture such processes, including previously unknown and unstudied processes. Particularly, we verified that the modified virtual crack close technique (MVCCT) accurately quantifies energy release rates for the complex configurations evaluated, further establishing the credibility of the numerical models.

The main objective of the current work is to demonstrate a previously unappreciated process that contributes to the understanding of the complex relationship between rock fabrics as well as the associated stress heterogeneity, natural fractures, and the containment of hydraulic fractures. The study does not intend to cover all factors that affect hydraulic fracture height growth. For instance, the interfaces between layers can slip and blunt hydraulic fracture's vertical growth (as speculated in Warpinski et al., 1998). This mechanism could further strengthen the stress barrier although usually bedding planes are under much higher confining stress than natural fractures are and therefore are less susceptible to slipping. Although no proppants are explicitly considered in the simulations, proppants are carried by the fracturing fluid during stimulation as a largely passive component. The sensitivity analysis on fluid viscosity to some extent has addressed proppants' effects through increased apparent viscosity of the fracturing fluid. Nevertheless, hydraulic fracture's vertical growth is a very complex matter; the current study demonstrates there are still a great deal of unknowns to be explored on this subject.

Nomenclature

h = fracture height, m
K_I = stress intensity factor of Mode I, MPa•$m^{0.5}$
K_{Ic} = critical stress intensity factor of Mode I, MPa•$m^{0.5}$
S_{hmin} = minimum horizontal *in situ* stress, Pa
S_{Hmax} = maximum horizontal *in situ* stress, Pa
p = fracture pressure, Pa
w_0 = aperture of fracture at zero effective stress, m
w_{ref} = aperture of fracture at reference effective stress, m
σ'_n = normal contact stress, Pa
$\Delta\sigma$ = stress difference, Pa

Acknowledgments

This manuscript has been authored by Lawrence Livermore National Security, LLC under Contract No. DE-AC52-07NA27344 with the US. Department of Energy. The United States Government retains, and the publisher, by accepting the article for publication, acknowledges that the United States Government retains a non-exclusive, paid-up, irrevocable, world-wide license to publish or reproduce the published form of this manuscript, or allow others to do so, for United States Government purposes. This work was funded by the Laboratory Directed Research and Development Program at LLNL under project tracking code 15-ERD-010. This document is LLNL report LLNL-JRNL-745501.

References

Bahorich, B., Olson J., and Holder, J. 2012. Examining the Effect of Cemented Natural Fractures on Hydraulic Fracture Propagation in Hydrostone Block Experiments. SPE Annu. Tech. Conf. Exhib. San Antonio, Texas. SPE-160197-MS. https://doi.org/10.2118/160197-MS

Bandis, S.C., Lumsden, A.C., Barton, N.R. 1983. Fundamentals of rock joint deformation. Int. J. Rock Mech. Min. Sci. 20 (6): 249–268. https://doi.org/10.1016/0148-9062(83)90595-8

Banks-Sills, L. 1991. Application of the Finite Element Method to Linear Elastic Fracture Mechanics. ASME. Appl. Mech. Rev. 44 (10): 447-461. https://doi.org/10.1115/1.3119488.

Barton, N., Bandis, S., Bakhtar, K. 1986. Strength, deformation and conductivity coupling of rock joints. Int. J. Rock Mech. Min. Sci. 22 (3), 121–140. https://doi.org/10.1016/0148-9062(85)93227-9

Belytschko, T., Ong, J.S., Liu, W.K., Kennedy, J.M. 1984. Hourglass control in linear and nonlinear problems. Computer Methods in Applied Mechanics and Engineering, 43(3): 251-276. https://doi.org/10.1016/0045-7825(84)90067-7.

Carlson, E. S., Mercer, J. C. 1991. Devonian Shale Gas Production: Mechanisms and Simple Models. Society of Petroleum Engineers. SPE Journal 43 (4). https://doi.org/10.2118/19311-PA

Chen, Z., Jeffrey, R. G., Zhang, X. and Kear, J. 2017. Finite-Element Simulation of a Hydraulic Fracture Interacting With a Natural Fracture. SPE Journal 22 (1): 219-234. https://doi.org/10.2118/176970-PA

Chuprakov, D., Prioul, R. 2014. Injection-Sensitive Mechanics of Hydraulic Fracture Interaction with Discontinuities. Rock Mechanics and Rock Engineering 47 (5): 1625–1640. https://doi.org/10.1007/s00603-014-0596-7

Cook, N.G.W. 1992. Natural joints in rock: Mechanical, hydraulic and seismic behaviour and properties under normal stress. Int. J. Rock Mech. Min. Sci. 29 (3): 198—223. https://doi.org/10.1016/0148-9062(92)93656-5

Eaton, B.A. 1969. Fracture gradient prediction and its application to oilfield operations, J. Petrol. Tech., October, 1353-1360.

Engelder, T. 1993, *Stress regimes in the lithosphere*. Princeton University Press. p. 492.

Engelder, T., Lash, G.G. and Uzcátegui, R.S. 2009. Joint sets that enhance production from Middle and Upper Devonian gas shales of the Appalachian Basin. AAPG bulletin, 93(7): 857–889. https://doi.org/10.1306/03230908032

Fu, P., Johnson, S. M. and Carrigan, C. R. 2013. An explicitly coupled hydro-geomechanical model for simulating hydraulic fracturing in arbitrary discrete fracture networks. Int. J. Numer. Anal. Meth. Geomech., 37: 2278–2300. https://doi.org/10.1002/nag.2135

Fu, P., Cruz, L., Moos, D., Settgast, R. R. and Ryerson, F. J. 2015. Numerical investigation of a hydraulic fracture bypassing a natural fracture in 3D, 49th U.S. Rock Mechanics/Geomechanics Symposium, San Francisco, CA, USA, 28 June-1 July. ARMA-2015-671.

Fu, W., Ames, B., Bunger, A. and Savitski, A. 2016. Impact of Partially Cemented and Non-persistent Natural Fractures on Hydraulic Fracture Propagation. Rock Mech Rock Eng 49: 4519–4526. https://doi.org/10.1007/s00603-016-1103-0

Gale, J., Laubach, S., Olson, J.E., Eichhubl, P., Fall, A. 2014. Natural Fractures in shale: A review and new observations. AAPG Bulletin, 98(11): 2165-2216. https://doi.org/10.1306/08121413151

Gu, H., Weng, X., Lund., J., Mark, M., Ganguly, U., Suares-Rivera, R. 2012. Hydraulic Fracture Crossing Natural Fracture at Nonorthogonal Angles: A Criterion and Its Validation. SPE Production & Operations 27(1). doi:10.2118/139984-PA.

Guo, B., Fu. P., Hao, Y., Peters, C., Carrigan, C. 2016. Thermal drawdown-induced flow channeling in a single fracture in EGS. Geothermics 61: 46-62. https://doi.org/10.1016/j.geothermics.2016.01.004

Guo, J., Zhao, X., Zhu, H., Zhang, X., Pan, R. 2015. Numerical simulation of interaction of hydraulic fracture and natural fracture based on the cohesive zone finite element method. Journal of Natural Gas Science and Engineering 25: 180-188. https://doi.org/10.1016/j.jngse.2015.05.008

Izadi, G., Gaither, M., Cruz, L., Baba C., Moos D., Fu P. 2015. Fully 3D Hydraulic Fracturing Model: Optimizing Sequence Fracture Stimulation in Horizontal Wells. Presented at the 49th US Rock Mechanics/Geomechanics Symposium, San Francisco, CA, USA, 28 June-1 July.

Jeffrey, R.G. and Settari, A. 1995. A Comparison of Hydraulic Fracture Field Experiments, Including Mineback Geometry Data, with Numerical Fracture Model Simulations. Presented at SPE Annual Technical Conference and Exhibition, Dallas, Texas, 22-25 October. https://doi.org/10.2118/30508-MS

Jeffrey, R.G. and Bunger, A. 2009. A detailed comparison of experimental and numerical data on hydraulic fracture height growth through stress contrasts. SPE Journal 14(3): 413–422. SPE-106030-MS. https://doi.org/10.2118/106030-MS

Kruger R. 2014. Virtual crack closure technique: history, approach, and applications. Applied Mechanics Reviews. 57(2):109–143. https://doi.org/ 10.1115/1.1595677

McClure, M. W. and Horne, R. N. 2013. *Discrete Fracture Network Modeling of Hydraulic Stimulation: Coupling Flow and Geomechanics*. Cham, Switzerland: Springer International Publishing.

Naceur, K.B. and Touboul, E. 1990. Mechanisms Controlling FractureHeight Growth in Layered Media. SPE Production Engineering 5(2): 142–150. https://doi.org/10.2118/16433-PA

Nolte, K.G. and Smith, M.G. 1981. Interpretation of FracturingPressures. J. Pet Tech 33(9): 1767-1775. SPE-8297-PA. https://doi.org/10.2118/8297-PA.

Pollard, D.D. and Aydin, A. 1984. Propagation and linkage of oceanic ridge segments. Journal of Geophysical Research, 89:10017–10028. https://doi.org/10.1029/JB089iB12p10017

Potluri, N., Zhu, D., Hill, A. 2005. The Effect of Natural Fractures on Hydraulic Fracture Propagation. SPE European Formation Damage Conference, 25-27 May, Sheveningen, The Netherlands. https://doi.org/10.2118/94568-MS

Raju, I.S. 1987. Calculation of strain-energy release rates with higher order and singular finite elements. Eng Fract Mech 28 (3): 251-274. https://doi.org/10.1016/0013-7944(87)90220-7

Renshaw, C. and Pollard D. 1995. An experimentally verified criterion for propagation across unbounded frictional interfaces in brittle, linear elastic materials. Int J Rock Mech Min Sci Geomech Abstr. 32: 237–249. https://doi.org/10.1016/0148-9062(94)00037-4

Sesetty, V. and Ghassemi, A. 2017. Complex Fracture Network Model for Stimulation of Unconventional Reservoirs. Presented at the 51st US Rock Mechanics/Geomechanics Symposium, San Francisco, CA, 25 June-28 June. ARMA-2017-0762.

Settgast, R., Johnson, S., Fu, P., Walsh, S. 2014. Simulation of hydraulic fracture networks in three dimensions utilizing massively parallel computing resources. SPE/AAPG/SEG Unconventional Resources Technology Conference, Denver, Colorado, USA. https://doi.org/10.15530/urtec-2014-1923299

Settgast, R, Fu, P, Walsh, S, White, J, Annavarapu, C, Ryerson, F. 2017. A fully coupled method for massively parallel simulation of hydraulically driven fractures in 3-dimensions. International Journal of Numerical and Analytical Methods in Geomechanics, 41(5): 627--653. https://doi.org/10.1002/nag.2557

Simonson, E.R., Abou-Sayed, A. S., and Clifton, R. J. 1978. Containment of Massive Hydraulic Fractures. SPE J. 18 (1): 27–32. SPE-6089-PA. https://doi.org/10.2118/6089-PA.

Sherman, C., Aarons, L.R., Morris, J., Johnson, S., Savitski, A., and Geilikman, M. 2015. Finite Element Modeling of Curving Hydraulic Fractures and Near-Wellbore Hydraulic Fracture Complexity. Presented at 49th US Rock Mechanics/Geomechanics Symposium, San Francisco, CA, USA, 28 June-1 July 2015.

Tada, H., Paris, P., Irwin, G. 2000. The Stress Analysis of Cracks Handbook, Third Edition. Wiley-Blackwell. https://doi.org/10.1115/1.801535

Taleghani, A., Olson, J. 2013. How Natural Fractures Could Affect Hydraulic-Fracture Geometry. SPE J. 19 (1): 161-171. SPE-167608-PA. https://doi.org/10.2118/167608-PA.

Warpinski, N.R., Clark, J.A., Schmidt, R.A., and Huddle, C.W. 1982a. Laboratory Investigation on the Effectof In-Situ Stresses on Hydraulic Fracture Containment. SPE J. 22 (3): 333-340. SPE-9834-PA. https://doi.org/10.2118/9834-PA.

Warpinski, N.R., Schmidt, R.A., and Northrop, D.A. 1982b. In-Situ Stresses: The PredominantInfluence on Hydraulic Fracture Containment. J. Pet Tech 34 (3): 653-664. SPE-8932-PA. https://doi.org/10.2118/8932-PA.

Warpinski, N.R. and Teufel, L.W. 1987. In-Situ Stresses: The PredominantInfluence on Hydraulic Fracture Containment. J. Pet Tech 39 (2): 209-220. SPE-13224-PA. https://doi.org/10.2118/13224-PA.

Warpinski, N.R., Branagan, P.T., Peterson, R.E., Wolhart, S.L. 1998. An interpretation of m-site hydraulic fracture diagnostic results. SPE Rocky Mountain Regional/Low-permeability Reservoirs Symposium, Denver, Colorado, 5-8 April. SPE-39950-MS. https://doi.org/10.2118/39950-MS

Weng, X., Kresse, O., Cohen, C. E., et al. 2011. Modeling of Hydraulic Fracture Network Propagation in a Naturally Fractured Formation. SPE Production & Operations, 26 (4): 368-380. SPE-140253-PA. https://doi.org/10.2118/140253-PA

Wu, K., Olson, J. 2016. Numerical Investigation of Complex Hydraulic-Fracture Development in Naturally Fractured Reservoirs. SPE Production & Operations, 31 (4) : 300–309. SPE-173326-PA. https://doi.org/10.2118/173326-PA

Zhang, X. and Jeffrey, R.G. 2008. Reinitiation or termination of fluid-driven fractures at frictional bedding interfaces. J Geophys Res., 113:1–16. https://doi.org/10.1029/2007JB005327

Zhang, F., Dontsov, E., Mack, M. 2017. Fully coupled simulation of a hydraulic fracture interacting with natural fractures with a hybrid discrete-continuum method. Int. J. Numer. Anal. Meth. Geomech, 41:1430–1452. https://doi.org/10.1002/nag.2682

Zhou, J., Huang, H., and Deo, M. 2015. Modeling the Interaction between Hydraulic and Natural Fractures Using Dual-Lattice Discrete Element Method. Presented at the 49th US Rock Mechanics/Geomechanics Symposium, San Francisco, CA, 28 June-1 July. ARMA-2015-507.

Zhou, J., Huang, H., and Deo, M. 2016. Simulation of Hydraulic and Natural Fracture Interaction Using a Coupled DFN-DEM Model. Presented at the 50th US Rock Mechanics/Geomechanics Symposium, Houston, TX, 26-29 June. ARMA-2016-739.

Zhou, J., Huang, H., McLennan, J., Meakin, P., Deo, M. 2017. A Dual-Lattice Discrete Element Model to Understand Hydraulic Fracturing in a Naturally Fractured System. Hydraulic Fracturing Journal, 4(2): 66-82.

Zoback, M. D., Kohli, A., Das, I., Mcclure, M. W. 2012. The Importance of Slow Slip on Faults During Hydraulic Fracturing Stimulation of Shale Gas Reservoirs. SPE Americas Unconventional Resources Conference, Pittsburgh, Pennsylvania, 5-7 June. SPE-155476-MS. https://doi.org/10.2118/155476-MS